ATLAS

P. Albicocco (Ass. Tecn.), M. Antonelli(Resp.), C. Arcangeletti (dott.),
M.M. Beretta, H. Bilokon, S. Cerioni (Tech.),
V. Chiarella, M. Curatolo, R. Di Nardo,
M. Dreucci, B. Esposito, M. Gatta (Tech.),
C. Gatti, P.F. Laurelli, S. Lauciani(Tech.),
G. Maccarrone, A. Martini, G. Mancini(Ass. Ric.),
G. Nicoletti, G. Pileggi (Tech.), B. Ponzio(Tech.),
V. Russo(Tech.), A. Sansoni, M. Testa,
P. T. Vassilieva (Tech.), E. Vilucchi.

In collaboration with:
Centro di Calcolo:
M. Pistoni, D. Spigone

March 30, 2018

1 Introduction

In the 2015-2016 data taking ATLAS collected proton-proton collisions at 13 TeV center of mass energy corresponding to an integrated luminosity of about 36.1 fb^{-1}.
Our group contributed significantly to the analysis $H \rightarrow ZZ \rightarrow 4\ell$ and Higgs Prospects as will be described in the following.
These contributions have been made possible also thanks to the reliability and the tools available on the LNF Tier2 approved by the INFN.
In parallel with the data taking activity, including shifts and maintenance, we are deeply involved in two upgrade Phase I activities: the Fast TracK (FTK) for the upgrade of the trigger system, and the new Small
Wheel for the upgrade of the muon system.
In addition we are strongly involved also to the upgrade Phase II activity concerning the Inner Tracker (ITk).

2 Tier-2

During the year 2017 the Frascati Tier-2 successfully and continuously performed all the typical activities of an ATLAS Tier-2: Monte Carlo production and users and physics groups analysis; maintaining the site efficiency above 90% as always.
During the year, the Tier-2 farm has grown to 26 kHEPSPEC of computing power and about 1.7 PB of disk space. Moreover, in addition to the following Virtual Organizations (VO), LHC VOs, Belle, CTA and KM3Net, a new experiment has become part of the Tier-2 farm: PADME.
This experiment, hosted in Frascati, will use the storage system of the Tier-2 computing center for raw, MC and reconstructed data, and will run MC, reprocessing and analysis jobs in the Tier-2 cluster, with pledged resources, in full collaboration with the Tier-2's staff.
Among the most significant activities that involved the Tier-2 staff we can also mention the role of VO manager for ATLAS VO and software VO manager for KM3Net VO. These activities are of primary importance for the experiments, in fact, one of them is also recognized as in kind contribution of the Italian group.
Finally, for what concern the Grid middleware, during 2017 the Tier-2 continued to host the testbed of the DPM service (Disk Pool Manager) for the DPM international collaboration, regularly testing the updates and experimenting new technologies, such as new cache systems, in collaboration with the Italian ATLAS Tier-2 federation staff.

3 Particle Flow reconstruction and pile-up suppression

The pile-up conditions for the current Run2 are expected to be up to 80 mean interactions per bunch crossing. They induce serious degradation of the jets and $\not{E}_T$ resolutions and increase in fake rate contamination from pile-up jets. To face the future unprecedented pile-up conditions a Particle-Flow reconstruction has been revisited and developed within the collaboration since 2014. A paper has been published [1]. This kind of reconstruction can maximally mitigate pile-up effects by exploiting the correlations among the inner detector and the calorimeter. Through the association between tracks and calorimeter deposits and the track pointing to the interactions vertices, calorimeter energy deposits coming from pile-up interactions can be removed in the jets and $\not{E}_T$ reconstruction. Large improvements in resolutions and fake rate reduction can be therefore achieved. Figure 1 (top) shows the fractional

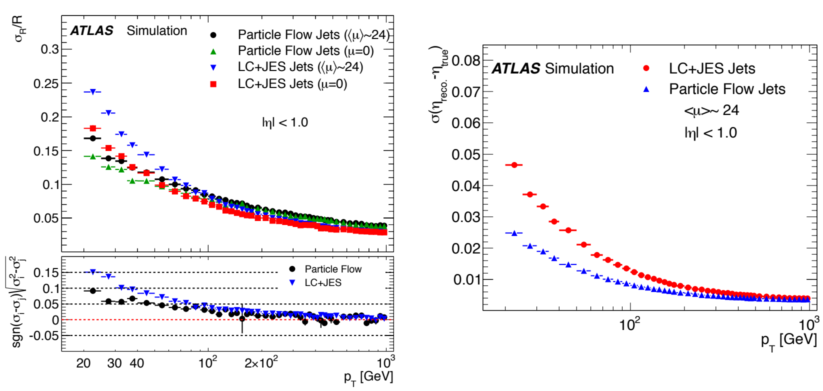

Figure 1: Left: The resolutions of calorimeter and particle flow jets determined as a function of p_{T} in Monte Carlo dijet simulation, compared with no pile-up and at $< \mu > \sim 24$. The quadratic difference in the resolution with and without pile-up is shown in the lower panel. Right: the angular resolution measured in Monte Carlo events.

p_T resolution of calorimeter based jets and Particle-Flow jets, with no pile-up and conditions similar to 2012 running. The bottom of figure 1 shows the resolution on the η direction versus the truth p_T of the jet. The algorithm has been integrated into the ATLAS software framework for Run 2 and is now available for use in physics analyses. The performance of the $\not{E}_T$ reconstruction with 2017 data are shown in Fig. 2.

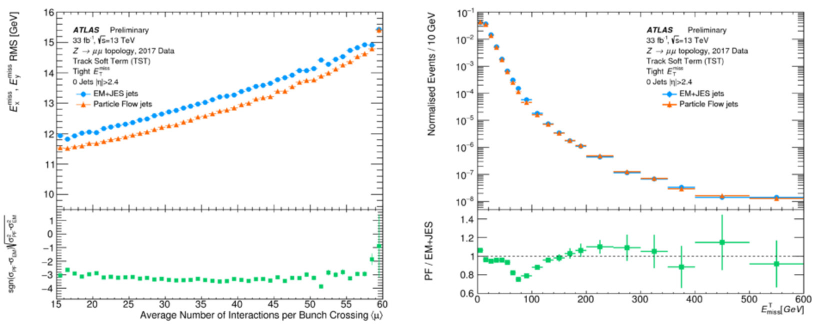

Figure 2: Left: $\not{E}_T$ resolution as a function of the average number of interactions per bunch crossing $< \mu >$ (left) and the $\not{E}_T$ distribution (right) are shown for 2017 data with a $Z \to \mu\mu$ selection applied. Different jet collections are use: calibrated jets built from electromagnetic scale topoclusters (EM+JES) and calibrated jets built from particle flow reconstruction (Particle Flow)

4 Jet/Etmiss performance of ITk for Phase-II upgrade

After the "Phase-I" upgrade in 2018, the LHC will undergo a "Phase-II" upgrade in 2023, to deliver the instantaneous luminosity of $\sim 7.5 \times 10^{34} cm^{-2} s^{-1}$, more than a factor 10 beyond its design value, corresponding to unprecedented pile-up conditions with an a average of 200 interactions per crossing. The ATLAS detector will be upgraded to maintain its capabilities. In particular the Inner Detector, with acceptance up to $|\eta| < 2.5$, will be substituted by a new, all-silicon Inner Tracker (ITk), whose acceptance will be $|\eta| < 4.0$.

4.1 Jet/E_{T}^{miss} offline reconstruction performance

There is tremendous potential for improved performance for jets and $\not{E}_T$ in the very forward region. Tracking information can be used by tagging pile-up jets in the forward region as has been done in the central region for Run I and Run II. Forward pile-up jets rejection induces an improvement in $\not{E}_T$ as well. The variable used to study the forward pile-up jet tagging is $R_{pT} = \frac{\Sigma_k p_T^{trk_k}(PV_0)}{p_T^{jet}}$ which computes the scalar sum of the p_T of the charged tracks associated with a particular jet, which are also associated with the primary vertex (PV0), and normalizes this to the p_T of the relevant jet. The rejection of pile-up jets versus the efficiency of the R_{pT} cut for hard-scatter jets is shown in Figure 3, left. The $\not{E}_T$ resolution as a function of the local pile-up density is shown in Figure 3, right. More information are in [2].

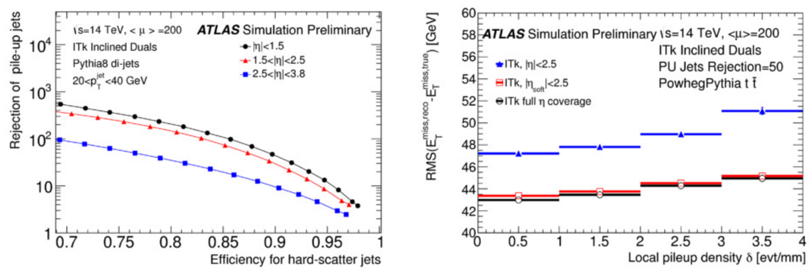

;

Figure 3: Left: The rejection of pile-up jets as a function of the efficiency for hard-scatter jets with $20 < pT < 40$ GeV p_T using the R_{pT} discriminant in di-jet events with an average of 200 pile-up events. Right: The resolution of $\not{E}_T$ in Monte Carlo $t\bar{t}$ events with an average of 200 pile-up events as a function of the local pile-up vertex density around the hard-scattering vertex, for three different $\not{E}_T$ definitions. The first (blue) considers only tracks in the region $|\eta| < 2.5$ for both pile-up jet rejection and soft-tracks not belonging to jets. The second uses tracks for pile-up jet rejection up to $|\eta|$ of 4 (red). The third uses tracks for pile-up jet rejection and soft-tracks up to $|\eta|$ of 4 (black).

4.2 Jet online Reconstruction performance: inclusive VBF trigger

The proposed ITk acceptance up to $|\eta|$ of 4.0 provides an opportunity to extend various triggers to include the forward region through regional or full-detector tracking. A calorimeter-only forward electron trigger is expected to have a high trigger rate due to the coarser calorimeter segmentation and high pile-up in the forward region. Such a trigger would therefore need to apply a high p_{T} threshold. To aid the performance of hadronic triggers, track-based pile-up suppression techniques have been developed. A study has been conducted to implement an inclusive VBF Higgs trigger and the impact of the forward tracking provided by the ITk system, has been addressed. A candidate selection requires two trigger jets separated in pseudo-rapidity by $|\Delta\eta| > 2.5$. They are further required not to be back-to-back as in dijet production ($|\Delta\phi| < 2.5$). The results show that an acceptance of 6.6% for all Higgs bosons produced by the VBF mechanism can be achieved with a jet p_{T} requirement of 75GeV corresponding to a Level-0 rate of 33 kHz, which can be reduced to ∼5 kHz by requiring the jets to be consistent with a common z vertex using regional tracking. The cross-section for the VBF process at $\sqrt{s} =$ 14 TeV is 4.28 pb , compared to the $WH, W \to l\nu$ cross-section times branching fraction of 0.34 pb and 0.067 pb for $ZH, Z \to ll$. The VBF inclusive trigger has comparable sensitivity to WH and far exceeding ZH. More detailed information can be found in [3].

5 ITk outer-endcap construction

The ITk detector comprises two subsystems: a Strip Detector surrounding a Pixel Detector. The ITk layout is shown in Fig.4, left. The Strip Detector (blue), covering $|\eta|$ <2.7, is complemented by a 5 layer Pixel Detector (red) extending the coverage to $|\eta| < 4$. The pixel end-cap system is designed to supply a minimum of at least 9 hits from the end of the strip coverage in pseudorapidity to $|\eta| = 4$. The novel concept is the end-cap ring system, where layers of pixel rings extend the coverage in z and allow routing of the service separately along each ring layer. Each ring can be individually placed to optimise the coverage. A Geant4 geometry model of the outer end-cap is shown in Fig.4, right. More information are in [2]. LNF is involved in the construction of one outer endcap of the ITk Pixel detector, being one the integration site. A 3d model of one outer endcap is shown in Fig.5, left. Each layer of rings is supported by a 0.4mm carbon fibre cylinder shell, along which services for the rings are routed. Each ring is constructed from two half-rings, each covering just over half of the ϕ coverage of the entire ring (Fig.5, right). The two half rings in a pair are separated in z by 10 mm, to allow them to overlap in ϕ such that each ring is hermetic for $p_{\mathrm{T}} = 1$ GeV primary particles. The pixel services (cables, coulding pipes, data lines) are routed from their sources out to Pixel Patch-Panel 1 (PP1). LNF is involved in the design, prototyping and construction of the PP1.
Publications, internal documents and public presentations:

- ATLAS Collaboration, "Jet Reconstruction and Performance Using Particle Flow with the ATLAS Detector",Eur. Phys. J. C 77 (2017) 466
- ATLAS Collaboration, "Technical Design Report for the ATLAS ITk Pixel Detector", ATL-COM-ITK-2017-073
- ATLAS Collaboration, "ATLAS Trigger and Data Acquisition Phase-II Upgrade Technical Design Report", ATL-COM-DAQ-2017-185
- ATLAS Collaboration,"Expression of Interest: A High-Granularity Timing Detector for ATLAS Phase-2 Upgrade", ATL-COM-LARG-2017-049
- ATLAS Collaboration, "Performance of missing transverse momentum reconstruction in 2015 data", submitted to EPJC

Responsabilities in ATLAS

- Convener of the Higgs Prospects analysis group (April 2017 - April 2019)
- Responsible of Data Quality of offline E_T^{miss} (April 2015 - current)

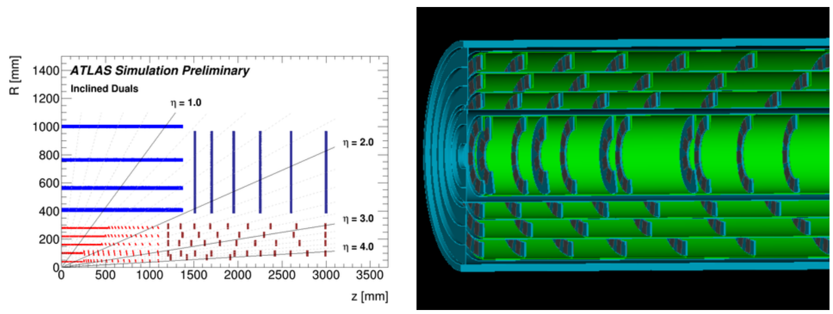

Figure 4: Left: Schematic layout of the ITk. Here only one quadrant and only active detector elements are shown. The horizontal axis is the axis along the beam line with zero being the interaction point. The vertical axis is the radius measured from the interaction region. The outer radius is set by the inner radius of the barrel cryostat that houses the solenoid and the electromagnetic calorimeter. Right: Geant4 geometry model of the inner and outer endcap structures with its' ring support for modules.

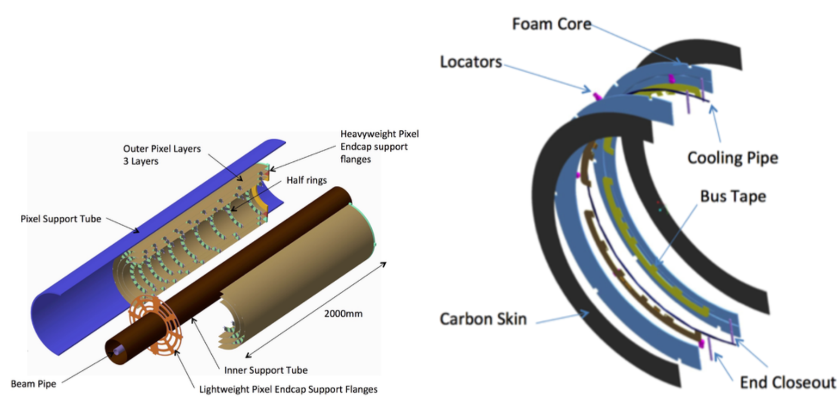

Figure 5: Left: Exploded 3D drawing of one Outer End-cap. Right: Exploded view and view of the surface of a half-ring

References

[1] ATLAS Collaboration, "Jet Reconstruction and Performance Using Particle Flow with the ATLAS Detector", Eur. Phys. J. C 77 (2017) 466

[2] ATLAS Collaboration, "Technical Design Report for the ATLAS ITk Pixel Detector", ATL-COM-ITK-2017-073

[3] ATLAS Collaboration, "ATLAS Trigger and Data Acquisition Phase-II Upgrade Technical Design Report", ATL-COM-DAQ-2017-185

6 FTK

The trigger is a fundamental part of any experiment at hadron colliders. It is needed to select on-line the interesting low cross-section physics from the huge QCD background. Experience at high luminosity hadron collider experiments shows that controlling trigger rates at high instantaneous luminosity can be extremely challenging. As the luminosity increases, physics goals change in response to new discoveries, and detector ageing. It is thus essential that the trigger system be flexible and robust, and redundant and significant operating margin. Providing high quality track reconstruction over the full ATLAS Inner Detector by the start of processing in the level-2 computer farm can be an important element in achieving these goals. With the goal to improve and make more robust the ATLAS trigger, during summer 2007 the group joined the Fast-Track (FTK) proposal for A hardware track finder for the ATLAS trigger. This is a proposal to build a hardware track finder as an upgrade to the ATLAS trigger. It will provide global reconstruction of tracks above 1 GeV/c in the silicon detectors, with high quality helix parameters, by the beginning of level-2 trigger processing. FTK can be particularly important for the selection of 3rd-generation fermions (b and τ). These have enormous background from QCD jets, which can be quickly rejected in level-2 if reconstructed tracks are available early. This RD proposal was completed with the submission of the FTK Technical Proposal that was finally approved by the ATLAS collaboration meeting in June 2011 [**?**].
Under the FTK context we contributed in the development and test of the Associative Memory (AM) chips for track detection and the FTK Input Mezzanines (IMs) boards for hit information clustering.

6.1 FTK Input Mezzanines

The FTK IMs boards receive data to be processed from the detectors Read Out Drivers (RODs) over 380 S-Link for a total input rate of $760Gbps$. Each board receives data over four optical links at $2Gbps$, performs an early reduction of the data to optimize the subsequent FTK processing and transmits forward the clustered data by a $200MHz\ DDR$ signalling over 16 LVDS pairs.
Due to the high occupancy of the IBL ATLAS pixel layer, the previous version of the FTK IM board based on Xilinx Spartan6 FPGA could not process all the data coming from the detector. We have developed this board together with FTK Japanese group of Waseda University. As responsible of this board the FTK collaboration ask us to develop a new version of the FTK IM based on a Xilinx Artix7 FPGA. This is a more recent and powerfull FPGA.
The new board have been designed in 2014, Figure 6.
During 2017 the firmware of the Artix-7 IM has been constantly kept updated. The main activities has been the maintenance of the mezzanine with problems.

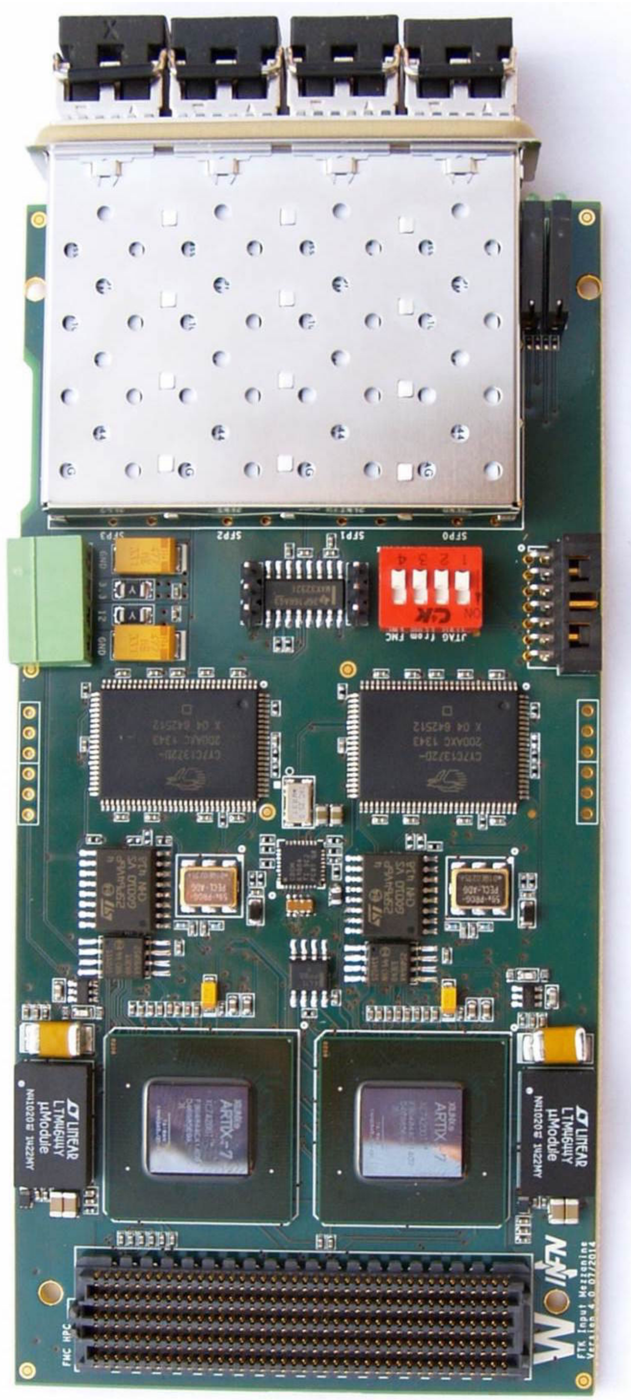

Figure 6: Artix7-IM

6.2 FTK AMCHIP06 test

In 2017 was started the AMchip06 mass production test at Microtest. LNF is involved in the test of this chip with these items:

- design a new test board without low drop voltage regulator;
- organizing and following the mass production test with external company.

In the following paragraph the listed items will be described.

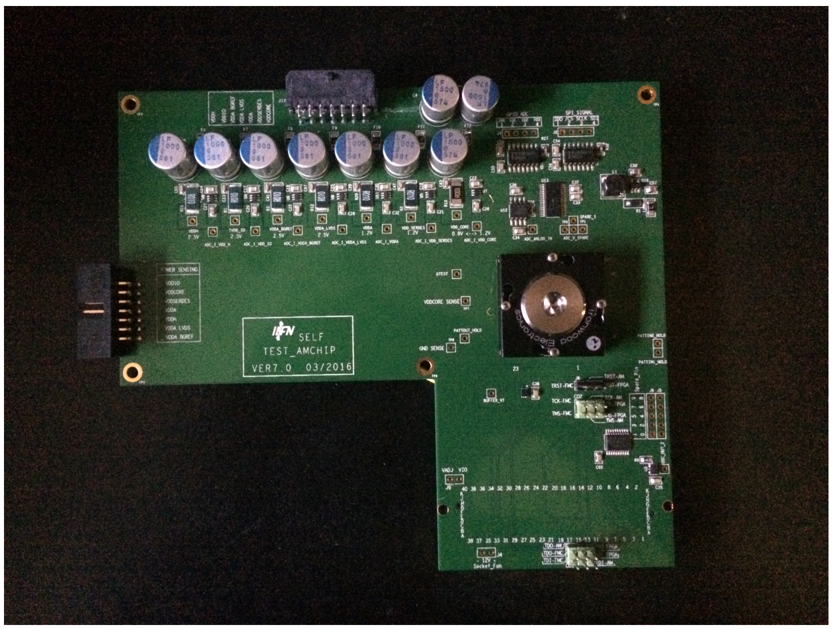

Figure 7: New test board for the AMchip06

The test board for the Amchip06 was re-designed to be compatible with new socket with mechanical spring contacts. The previous socket, with elastomer contacts, has shown reliability problems after few thousands of tested components (usually we have problems after 2000 components tested). We have to test about 20000 chips, so we have decided to change the socket with a more riliable and expensive one, in order to guarantee the correct level of reliability in the test results.
The specification used to design the board was the following:

- FMC HPC connector
- On Board 100MHz clock

- FMC alternative clock distribution
- 12 differencial high speed (2.5 GHz) lines
- On board power supply current and voltage monitor

The board designed with all features highlighted are shown in the picture 7 We are constantly in contact with the company in charge of the tests to give help in maintenance of the test system.

7 New Small Wheel upgrade project: MicroMegas [1], [2]

MicroMegas (MM) chambers is an abbreviation for MICRO MEsh GASeous Structure and it is an innovative design concept for Micro-Pattern Gaseous Detectors first introduced by Charpak and Giomataris during the 1990s.
These chambers have been chosen as new precision tracking detectors for the upgrade of the forward muon spectrometer of the ATLAS experiment at the Large Hadron Collider (LHC) during the second long shut-down of the LHC. MicroMegas are gas detectors in which a 5 mm gap between two parallel electrodes is filled with a $93:7$ $Ar:CO_2$ gas mixture and a thin metallic micromesh is placed between the two electrodes, held by pillars with a pitch of few millimetres and a height of about 128 μm. The drift electrode, with a -300 V voltage applied, and the mesh, which is grounded, define the drift region, where the ionization takes place and the low electric field ($\sim 600V/cm$) leads the produced electrons towards the mesh. Following the field lines the electrons enter the very thin amplification region between the mesh and the readout electrode, which is segmented into strips with a pitch of about 400 μm, where a $\sim$ $500-600$ V voltage is applied. Due to the very high electric field ($\sim$ $40-50$ kV/cm) the electrons produce avalanches with a gain of the order of 10^4. The thin amplification gap allows a fast ions evacuation, which occurs in about 100 ns, and allows MM to operate in highly irradiated environments. MM chambers are designed to provide a space resolution below 100 μm and a tracking efficiency better than 95% per single plane.
The produced signal is then read by the readout strips capacitively coupled to the resistive ones in order to reduce the performance degradation due to discharges in the detector.
INFN is deeply involved in the Micromegas Chambers construction and testing of the new chambers at the LNF Cosmic Ray Stand. The experimental setup currently consists of two SiPM (Silicon PhotoMultipliers) for the trigger coincidence and two well tested Tmm Chambers [1] taken as reference.
The Signals from the read-out strips are read using APV25 front-end readout electronics which provides the collected charge as a function of the time in 25

[1] Tmm type bulk resistive MM with 10 cm × 10 cm active area, with strips 150 μm wide and with a pitch of 250 μm.

ns bins. By fitting the risetime of the distribution with an inverse Fermi-Dirac function, the time of the arrival of the signal, defined as the inflection point of the function, and the charge induced on the strip, defined as the maximum of the distribution subtracted by the baseline level, can be measured. For each strip i the time t_i and the charge q_i are therefore measured and clusters are reconstructed as groups of neighbouring strips according to dedicated clustering algorithms.

7.1 First MM prototypes

In the year 2016 the R&D process on the MicroMegas (MM) detector, the phase-1 upgrade of the Atlas Forward Muon Spectrometer, arrived to a conclusion with the Module 0 construction (Figure 8).

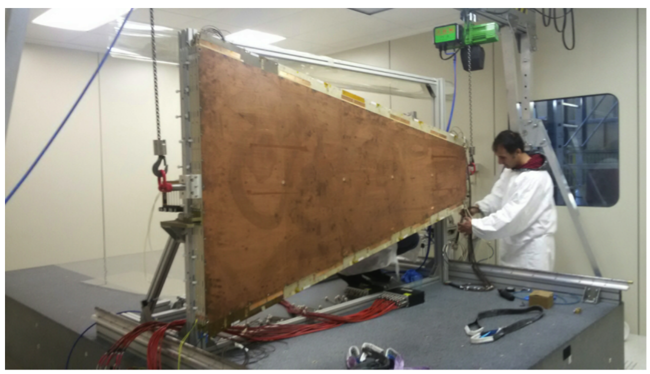

Figure 8: Completed Module 0 ready to be removed from the assembly tool.

The INFN collaboration, responsible for the SM1 chambers, built the Module 0 in April-May and, transported at Cern, tested in a high energy muon/pion SPS secondary beam (H8) (Figure 9).
The Italian MM group was the only one able to build their own Module 0 in the year 2016, the other three groups have done it in 2017.
Test results were satisfactory, resolution, both in precise coordinate and in the second coordinate, was close to the expectations, as the efficiency (Figure 10 and 11).
Test of mechanical integration of the SM1 Module 0 was also performed at Cern, showing that the detector is from the mechanical point of view even more stiff than foreseen in the simulation (Figure 12).
The module 0 went back to LNF in September to be re-opened to study in details the reasons for some HV instability seen during the test beam.
After this work, at the end of the year, many unstable sectors were fixed and the number of residual problematic ones was of the order of 10% related to the

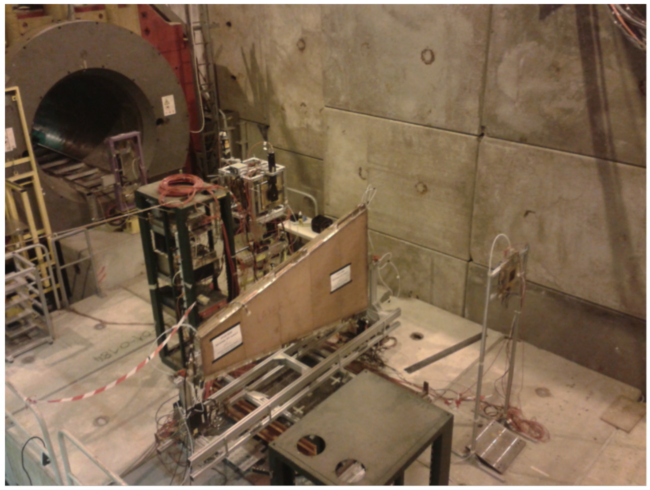

Figure 9: Test beam setup in the H8 SPS beam line, with SM1 Module 0.

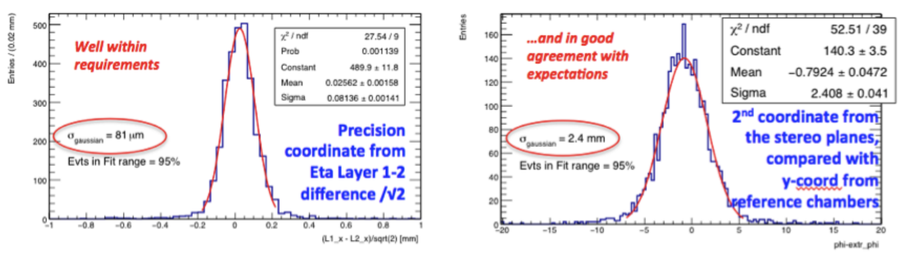

Figure 10: Module 0 resolutions obtained in the test beam.

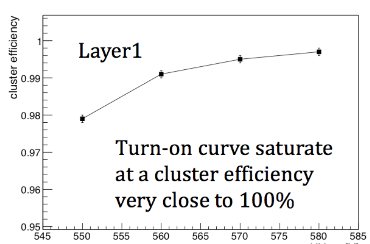

Figure 11: Turn On curve, efficiency Vs HV showing good efficiency, close to 1.

Figure 12: Mechanical simulation of the SM1 mounting in the Wheel. The yellow/black structure provided detector rotation in all possible final positions.

poor single PCB quality.
During 2017 the Mod0.5 has been constructed, assembled and tested at the CRS at LNF with the experimental setup described above and shown in Figure 13.

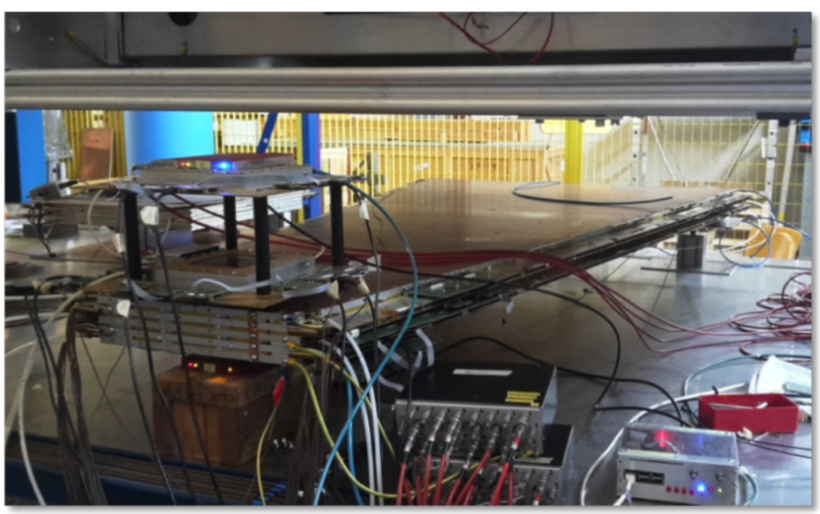

Figure 13: Experimental setup at the ATLAS LNF Cosmic Ray Stand.

The HV issues have been deeply investigated and a cleaning procedure has been refined to cope with that.
Preliminary results on the hardware efficiency show consistency with what expected and are shown in Figure 14.

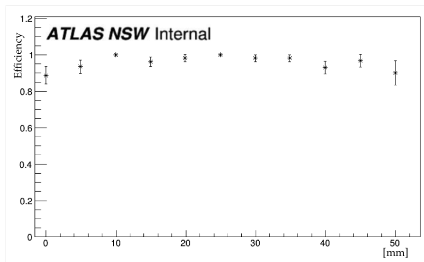

Figure 14: Hardware efficiency of the Mod0.5.

7.2 Production scheme

The NSW structure consist of 8 large sectors and 8 small sectors, with 2 modules per sector and 4 MM quandruplets.
MM chambers are therefore produced in 4 different shapes: LM1, LM2, SM1, SM2.
The production is distributed over different institutes and industries: Germany(SM2), France(LM1), Russia-Greece-CERN (LM2) and Italy is responsible for the SM1 construction.
The INFN Italian production is summarized as shown in Figure 15 and the construction is ongoing as sown in Table 16.

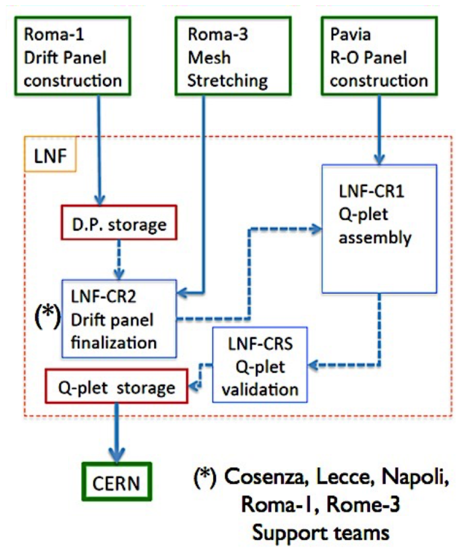

Figure 15: INFN production scheme of SM1.

	Ritmo di produzione	Frazione del totale
Pannelli di Drift (RM1)	1 panello/settimana	35/96
Mesh Stretchate (RM3)	4 meshes/settimana	37/128
Pannelli di Drift finalizzati (LNF CR2)	1 panello/settimana	19/96
Pannelli di RO – Eta (PV)	1 panello/2 settimane	1/32
Pannelli di RO – Stereo (PV)	1 panello/2 settimane	3/32
Quadrupletti (LNF CR1)	1 quadrupletto/2 settimane	1/32

Figure 16: Status of production of SM1.

8 Study on the properties of the Higgs boson in the $H \to ZZ^* \to 4l$ decay channel

In the 2015 and 2016 data taking at LHC, ATLAS collected proton-proton collisions at 13 TeV center of mass energy, corresponding to an integrated luminosity of 36.1 fb^{-1}.
Back on 4 July, 2012, the LHC experiments reported the evidence of an Higgs boson-like particle with a mass of about of 125 GeV and great interest has been posed on the measurements of its properties to assure whether it is the Standard Model (SM) Higgs boson or not. In this context, during the Run2 at LHC, with an increased center of mass energy of the collisions, the measurement of the Higgs properties remains one of the main goals of the physics program since hints of New Physics (NP) effects can be hidden in the Higgs sector. Deviations from the SM expectations could indicate exotic properties of the Higgs or presence of exotic particles in association with Higgs. Studies performed during Run1 showed that deviations from the SM expectations in the Higgs sector are small: the Higgs quantum numbers are measured to be $J^P = 0^+$ (alternative hypotheses are excluded with a 99.9% C.L.), its signal strength ($\mu = Ev_{obs}/Ev_{SM}$) and coupling measurements to vector bosons and fermions are found to be consistent with the SM with an accuracy of the order of 10%.
In the $H \to ZZ^* \to 4\ell$ final state, the first measurement in Run2 have been focusing on the Higgs boson coupling to SM particles. The measurement has been performed dividing the events in categories built depending on the characteristic of the event, aiming for discrimination between production modes. The measurement of the cross section per production mode has been performed, together with the measurement of the Higgs boson couplings to bosons and fermions.
In the SM, the Higgs boson is a $\mathcal{CP}$-even scalar particle ($J^{\mathcal{CP}} = 0^{++}$) and theories of physics BSM often require an extended Higgs sector featuring several neutral Higgs bosons. Such cases may include $\mathcal{CP}$-mixing in the Higgs boson interactions, which could result in observable differences in the kinematics of final-state particles produced in their decays, or from Higgs boson production, such as in VBF interactions.
The possible presence of BSM terms in the Lagrangian describing the spin-0 resonance is investigated describing the HVV vertex interaction in terms of an effective BSM $\mathcal{CP}$-odd and $\mathcal{CP}$-even operators and deriving limits on the corresponding BSM tensor couplings are derived. Our group contributed significantly to this studies ([3]) with fundamental contributions to the analysis and to the measurement of the Higgs boson properties in the $H \to ZZ^* \to 4\ell$ decay channel.

8.1 Cross section per production mode measurements

In order to measure the cross sections per production mode, categories enriched in each Higgs production mechanism have been defined 17.
The Higgs boson production cross section times the branching ratio of the decay into Z boson pairs, $\sigma \times BR(H \to ZZ^*)$, is measured in several dedicated mutually exclusive regions of the phase space based on the production process which are called production bins (Figure **??**). The bins are chosen in such a way that the measurement precision is maximized and at the same time possible BSM contributions can be isolated. All production bins are defined for Higgs bosons with rapidity $|y_H| < 2.5$ and no requirements placed on the particle-level leptons. Two sets of production bins are considered since a more inclusive phase-space region usually reduces the statistical uncertainty of the measurement but at the cost of a larger theoretical uncertainty. For the first set (Stage 0), production bins are simply defined according to the Higgs boson production vertex: gluon-gluon fusion (ggF), vector boson fusion (VBF) and associated production with top quark pairs (ttH) or vector bosons (VH), where V is a W or a Z boson. The bbH Higgs boson production bin is not included because there is insufficient sensitivity to measure this process with the current integrated luminosity. This production mode has an acceptance similar to gluon-gluon fusion, and their contributions are therefore considered together in the analysis. The sum of their contributions is referred to in the following as gluon-gluon fusion. For the second set (reduced Stage 1), a more exclusive set of production bins is defined. There are nine reconstructed event categories defined for the cross-section measurement, one of which is additionally split into two separate ones for the tensor structure studies to improve their sensitivity. For the crosssection measurement, there are also additional discriminating observables introduced in reconstructed event categories with a sufficiently high number of events. These observables are defined using dedicated boosted decision trees (BDTs). The expected number of SM Higgs boson events with a mass $m_H = 125.09$ GeV in the mass range $118 \leq m_{4l} \leq 129$ GeV for an integrated luminosity of $36.1 fb^1$ and $\sqrt{s} = 13$ TeV in each reconstructed event category, shown separately for each Stage-0 production bin (Figure **??**). The ggF and bbH contributions are shown separately but both contribute to the same (ggF) production bin. Statistical and systematic uncertainties are added in quadrature. Figure 19 shows the fraction of signal events in each category per production modes, showing the extreme purity of some categories. The ggF and bbH contributions are shown separately but both contribute to the same (ggF) production bin. The relation between N_k^{obs}, the observed number of events in each analysis categories (denoted as k), and the cross section in each truth bin σ_i^j (i denotes different production mechanisms and j denotes the index of a phase space or truth bin in the simplified template cross section binning scheme), can be expressed as

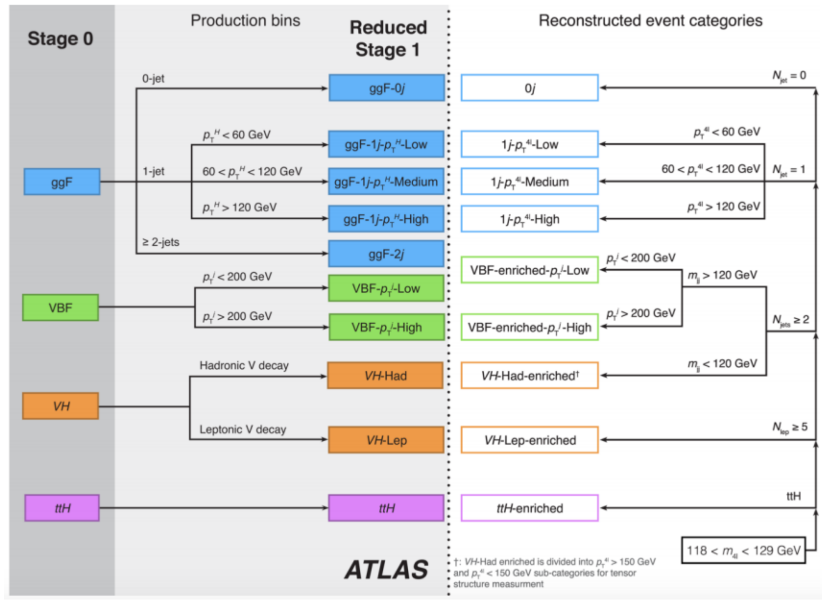

Figure 17: Event categorization scheme.

Reconstructed	SM Higgs boson production mode				
event category	ggF	VBF	*VH*	*ttH*	*bbH*
$0j$	25.9 ± 2.5	0.29 ± 0.09	0.253 ± 0.025	0.00025 ± 0.00019	0.29 ± 0.14
$1j$-$p_T^{4\ell}$-Low	8.0 ± 1.1	0.514 ± 0.034	0.230 ± 0.018	0.0007 ± 0.0005	0.09 ± 0.05
$1j$-$p_T^{4\ell}$-Med	4.5 ± 0.7	0.64 ± 0.09	0.227 ± 0.019	0.0010 ± 0.0005	0.026 ± 0.013
$1j$-$p_T^{4\ell}$-High	1.10 ± 0.24	0.27 ± 0.04	0.095 ± 0.007	0.00080 ± 0.00024	0.0036 ± 0.0018
VBF-enriched-p_T^j-Low	3.9 ± 0.8	2.03 ± 0.19	0.285 ± 0.024	0.065 ± 0.009	0.045 ± 0.023
VBF-enriched-p_T^j-High	0.33 ± 0.09	0.185 ± 0.024	0.050 ± 0.004	0.0159 ± 0.0027	0.00058 ± 0.00029
VH-Had-enriched-$p_T^{4\ell}$-Low	2.3 ± 0.5	0.169 ± 0.014	0.418 ± 0.023	0.022 ± 0.004	0.025 ± 0.013
VH-Had-enriched-$p_T^{4\ell}$-High	0.42 ± 0.09	0.048 ± 0.008	0.162 ± 0.005	0.0090 ± 0.0015	< 0.0001
VH-Lep-enriched	0.0129 ± 0.0018	0.00310 ± 0.00021	0.263 ± 0.018	0.038 ± 0.005	0.0009 ± 0.0005
ttH-enriched	0.050 ± 0.016	0.010 ± 0.006	0.0196 ± 0.0031	0.301 ± 0.032	0.0064 ± 0.0035
Total	47 ± 4	4.16 ± 0.23	2.00 ± 0.11	0.45 ± 0.05	0.49 ± 0.24

Figure 18: The expected number of SM Higgs boson events with a mass $m_H = 125.09$ GeV in the mass range $118 \leq m_{4l} \leq 129$ GeV for an integrated luminosity of $36.1 fb^1$ and $\sqrt{s} = 13$ TeV in each reconstructed event category.

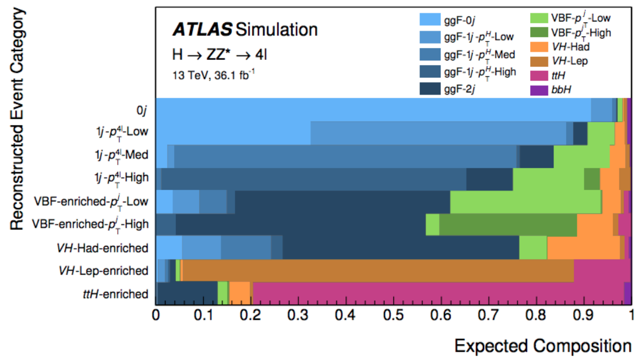

Figure 19: Signal composition in terms of the reduced Stage-1 production bins in each reconstructed event category.

follows:

$$\mathcal{N}_k^{\text{obs}} = \mathcal{L}_{\text{int}} \times \mathcal{BR}_{H\to ZZ^*\to 4\ell} \times \Big(\sum_{i=1}^{\mathcal{N}^{prod}} \sum_{j=1}^{\mathcal{N}^{i}_{bin}} \mathcal{A}^i_{kj}\sigma^j_i \Big) \tag{1}$$

where $\mathcal{L}_{\text{int}}$ is the integrated luminosity, $\mathcal{N}^{prod}$ is the number of Higgs production mechanisms, $\mathcal{N}^i_{bin}$ is the number of truth bins per Higgs production mechanism i, $\mathcal{A}^i_{kj}$ takes into account for detector response (trigger, reconstruction and identification efficiencies) for detecting the final state and the kinematic and geometric acceptance for the truth bin j of Higgs production mechanism i in the analysis category k.
Assuming that the relative signal fractions in each production bin are given by the predictions for the SM Higgs boson, the inclusive production cross section of

$$\sigma \times BR(H \to ZZ^*) = 1.73^{+0.24}_{0.23}(stat.)^{+0.10}_{0.08}(exp.) \pm 0.04(th.)pb = 1.73^{+0.26}_{0.24}pb \tag{2}$$

is measured in the rapidity range $|y_H| < 2.5$, compared to the SM prediction of

$$\sigma \times BR(H \to ZZ^*) = 1.34 \pm 0.09pb \tag{3}$$

The data are also interpreted in terms of the global signal strength, yielding

$$\mu = 1.28^{+0.18}_{0.17}(stat.)^{+0.08}_{0.06}(exp.)^{+0.08}_{0.06}(th.) = 1.28^{+0.21}_{0.19} \tag{4}$$

Results are extracted from fits to the data using the profile likelihood ratio. Figures 20 show the results in terms of cross sections per production mode respectively for the Stage0 and Stage1 cases.
The same categorization can be used for the measurements of coupling modifiers (κ) to SM particles within the k-framework interpretation. Figure 21 shows the interpretation in terms of coupling modifiers of the Higgs boson coupling to fermions (κ_f) and vector bosons (κ_V).

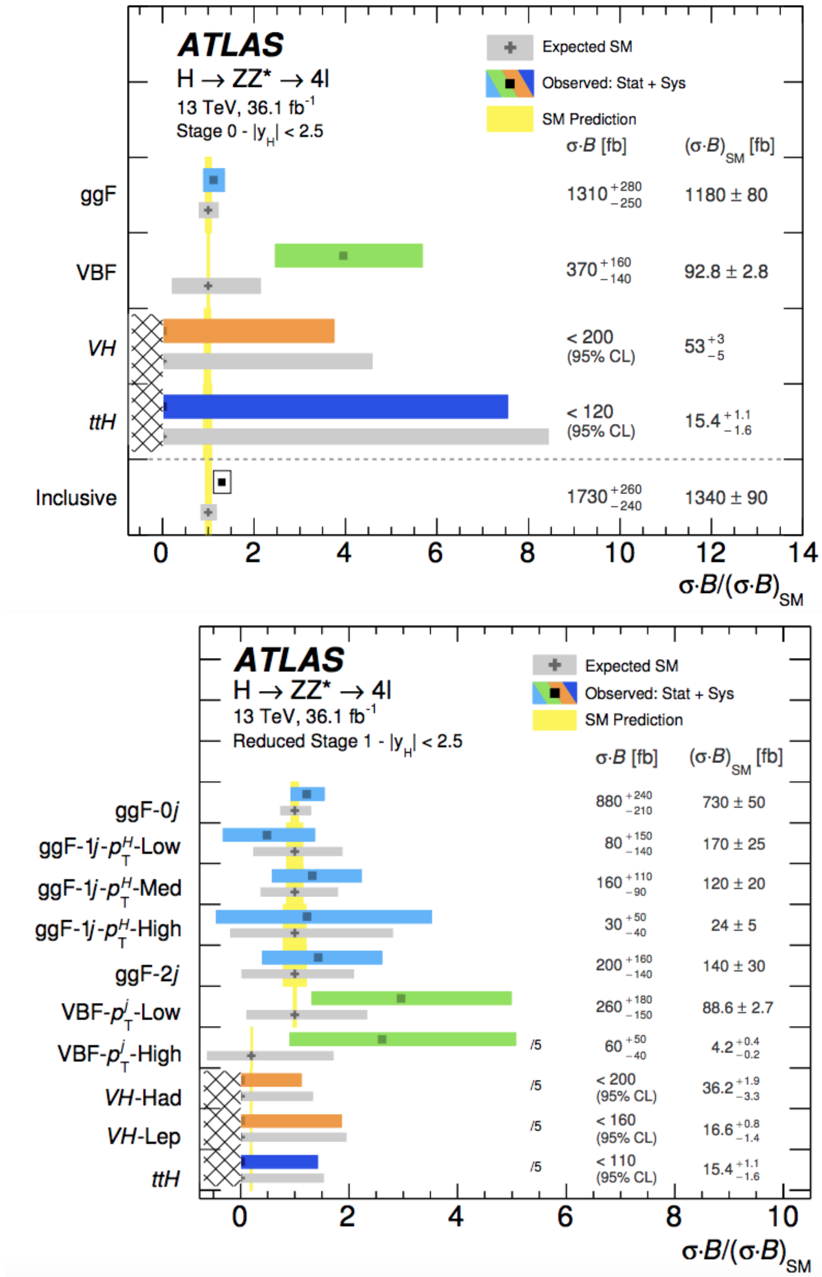

Figure 20: . The observed and expected SM values of the cross-section ratios $\sigma \times BR$ normalized by the SM expectation for the inclusive production and in the Stage0 and reduced Stage-1 production bins. Different colors for the observed results indicate different Higgs boson production modes. The hatched area indicates that the VH and ttH parameters of interest are constrained to positive values. For visualization purposes, the VBF-p_{Tj}-High value and the limits for the three reduced Stage-1 production bins VH -Had, VH -Lep and ttH are divided by a factor of five when shown normalized to $\sigma \times BR_{SM}$. The yellow vertical band represents the theory uncertainty in the signal prediction, while the horizontal grey bands represent the expected measurement uncertainty.

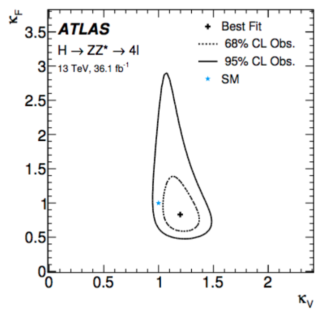

Figure 21: 2D likelihood scan of the κ_V and κ_F.

8.2 Effective Field Theory (EFT) interpretation

This study aims to use properties from the different production mechanisms and the $H \to ZZ^*$ decays to derive information on the $\mathcal{CP}$ nature of the Higgs boson.
Due to the fact that the VBF and VH production mechanisms are particularly sensitive to possible BSM contributions, an effective field theory (EFT) approach has been adopted in order to describe the interactions between the resonance and the SM vector bosons, following the Higgs boson characterisation model [5] [4].
Among all the possible scenarios, only the hypothesis that the observed resonance is a mixture of spin-0 $\mathcal{CP}$-even and/or $\mathcal{CP}$-odd states has been considered, meaning that, in the case of $\mathcal{CP}$ mixing, the Higgs boson would be a mass eigenstate, but not a $\mathcal{CP}$ eigenstate, implying $\mathcal{CP}$-violation in the Higgs sector.
In all cases, only one resonance with a mass of about 125 GeV is considered; it is also assumed that the total width of the resonance is small with respect to the typical experimental resolution of the ATLAS detector and the interference effects between the signal and SM backgrounds are negligible.
The Higgs Characterization model relies on an EFT approach which, by definition is only valid up to a certain energy scale Λ, set to 1 TeV to account for the experimental results obtained by the LHC and previous collider experiments that show no evidence of new physics at lower energy scales.
The model assumes that the resonance structure corresponds to one new boson, assuming that any other BSM particle exists at an energy scale larger than Λ.
The investigation of possible mixing between the Standard Model $\mathcal{CP}$-even and BSM $\mathcal{CP}$-even and $\mathcal{CP}$-odd contributions is performed, providing a study of the HVV Lagrangian tensor structure.
In the Higgs boson characterization model, the description of the spin-0 particle interaction with pairs of W and Z bosons is given through the

following interaction Lagrangian:

$$\begin{aligned}\mathcal{L}_0^V = \quad & \left\{c_\alpha \kappa_{\mathrm{SM}} \left[\tfrac{1}{2} g_{HZZ} Z_\mu Z^\mu + g_{HWW} W^+_\mu W^{-\mu}\right]\right. \\ & -\tfrac{1}{4}\tfrac{1}{\Lambda}\left[c_\alpha \kappa_{HZZ} Z_{\mu\nu} Z^{\mu\nu} + s_\alpha \kappa_{AZZ} Z_{\mu\nu} \tilde{Z}^{\mu\nu}\right] \\ & \left.-\tfrac{1}{2}\tfrac{1}{\Lambda}\left[c_\alpha \kappa_{HWW} W^+_{\mu\nu} W^{-\mu\nu} + s_\alpha \kappa_{AWW} W^+_{\mu\nu} \tilde{W}^{-\mu\nu}\right]\right\} X_0.\end{aligned} \tag{5}$$

where V^μ represents the vector-boson field ($V = Z, W^\pm$), the $V^{\mu\nu}$ are the reduced field tensors and the dual tensor is defined as $\tilde{V}^{\mu\nu} = \frac{1}{2}\varepsilon^{\mu\nu\rho\sigma}V_{\rho\sigma}$. The κ_{SM}, κ_{HVV} and κ_{AVV} denote the coupling constants corresponding to the interaction of Standard Model, BSM $\mathcal{CP}$-even and BSM $\mathcal{CP}$-odd spin-0 particles, represented by the X_0 field, with ZZ or WW pairs.
Other higher-order operators [4], namely the derivative operators, are not included in Equation 5 and have been neglected in this analysis. To ensure that the Lagrangian terms are Hermitian, these couplings are assumed to be real.
The mixing angle α allows for production of $\mathcal{CP}$-mixed states and implies $\mathcal{CP}$-violation for $\alpha \neq 0$ and $\alpha \neq \pi$, provided the corresponding coupling constants are non-vanishing: the following notation will be used hereafter: $s_\alpha = \sin\alpha$ and $c_\alpha = \cos\alpha$.
The Standard Model coupling strengths, g_{HVV}, are proportional to the square of the vector boson masses: $g_{HVV} \propto m^2_{Z/W}$.
To quantify the presence of BSM contributions in experimentally observed $H \to ZZ^*$ decay, the observed ratios of couplings κ_{AVV} and κ_{HVV} are measured for the $\mathcal{CP}$-mixing and anomalous $\mathcal{CP}$-even contribution scenarios, respectively.
All the models used in these studies are obtained by selecting the corresponding parts of the Lagrangian described in Equation 5 while setting all other contributions to zero. The custodial symmetry has been also imposed: in κ_{AVV} and κ_{HVV} $V = W, Z$.
The BSM terms described in Equation 5 are also expected to change the relative contributions of the vector-boson fusion (VBF) and vector-boson associated production (VH) processes with respect to the gluon-fusion (ggF) production process, which is predicted to be the main production mode for the SM Higgs boson at the LHC.
For large values of the BSM couplings, the VBF and VH production modes can have a significantly higher cross section due to the fact that the BSM couplings to W/Z bosons enter with the square power in the computation of the cross section. For the VBF and VH Higgs boson events decaying into 4ℓ final state the contribution of κ_{BSM} enters both in production and decay vertexes; while for the ggH, ttH and bbH, κ_{HVV} and κ_{AVV} can only enter in the decay vertex as shown in Figure 22. The expected results for the tensor coupling analysis are obtained using an Asimov data set built from Standard Model events. The tensor couplings have been studied separately, fixing in the Lagrangian the SM component to its expectation ($\kappa_{SM} = 1$).
The likelihood expected distribution of Figure **??** is symmetric since the cross

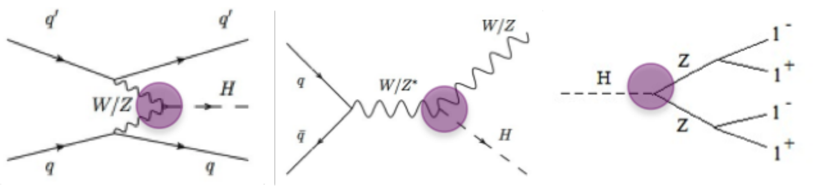

Figure 22: Interaction vertices involving the κ_{HVV} and κ_{AVV} BSM coupling considered.

section scales at the same rate for negative and positive values of κ_{AVV}; a small asymmetry is therefore seen due to the difference in the categorization among positive and negative values of κ_{AVV}. Table **??** shows a comparison

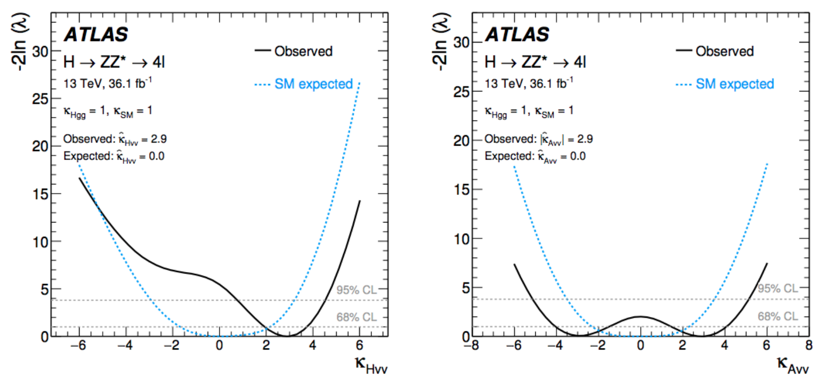

Figure 23: Observed (black) and expected (blue) results for the κ_{HVV} (left) and κ_{AVV} (right) analysis of the tensor coupling structure of the Higgs Boson.

between the observed and expected limits at 95% CL for the tensor couplings chosen in this analysis.

BSM coupling $\kappa_{\rm BSM}$	Fit configuration	Expected conf. inter.	Observed conf. inter.	Best-fit $\hat{\kappa}_{\rm BSM}$	Best-fit $\hat{\kappa}_{\rm SM}$	Deviation from SM
κ_{HVV}	$(\kappa_{Hgg}=1,\ \kappa_{\rm SM}=1)$	$[-2.9, 3.2]$	$[0.8, 4.5]$	2.9	-	2.3σ
κ_{HVV}	$(\kappa_{Hgg}=1,\ \kappa_{\rm SM}$ free)	$[-3.1, 4.0]$	$[-0.6, 4.2]$	2.2	1.2	1.7σ
κ_{AVV}	$(\kappa_{Hgg}=1,\ \kappa_{\rm SM}=1)$	$[-3.5, 3.5]$	$[-5.2, 5.2]$	±2.9	-	1.4σ
κ_{AVV}	$(\kappa_{Hgg}=1,\ \kappa_{\rm SM}$ free)	$[-4.0, 4.0]$	$[-4.4, 4.4]$	±1.5	1.2	0.5σ

Figure 24: Expected and observed confidence intervals at 95% CL on the κ_{HVV} and κ_{AVV} coupling parameters, their best-fit values and corresponding compatibility with the SM expectation, as obtained from the negative log-likelihood scans performed with $36.1 fb^1$ of data at $\sqrt{s} = 13$ TeV.

8.3 Background studies in the ttH category

The study of the associated production of the Higgs boson with a top quark pair in $H \to ZZ^* \to 4l$ decay channel has been performed using the Run 2 data-set taken in the year 2015 and 2016, corresponding to an integrated luminosity of 36.1 fb^{-1}, by the ATLAS detector at collision center-of-mass energy of 13 TeV.
The search for the associated production of the Higgs boson with a top quark pair (ttH) is very useful to study the Higgs couplings with the top quark and possible extension of the Standard Model in the top quark sector, because the top quark is the most strongly-coupled SM model particle to the Higgs boson due its large mass ($\sim$ 170 GeV). This production mode permits a direct measurement of the top-Higgs Yukawa coupling and can highlights effects of New Physics in process like the gluon-gluon fusion, in which this couplings appears at the next to leading order in a loop.
The study of this process has been developed in a preliminary analysis of the $H \to ZZ^* \to 4l$ decay channel, followed by a detailed study of the ttH production mode in this decay channel. In this channel the main sources of background events are the continuum $(Z^{(*)}/\gamma^*)(Z^{(*)}/\gamma^*)$ production, that is the irreducible component, and the *Z+jets* and $t\bar{t}$ production, that represents the reducible component. Then a cut-based analysis has been performed, in which a set of kinematic and topological selections has been applied to the data sample to isolate the signal events from these sources of background. In Figure 25 the inclusive distribution of the $4l$ system invariant mass are presented, comparing the background and signal expectation with the data set recorded at $\sqrt{s}$=13 TeV for an integrated luminosity of 36.1 fb^{-1} and the m_{34} distribution for selected events in the mass range 115-130 GeV, as a function of the invariant mass m_{12}, and their projections. In the plot on the m_{12}, m_{34} distributions, the Z mass constraint kinematic fit is not applied. The result of the event selection show no significant deviations with respect to the Standard Model predictions within the errors, dominated by the statistics, due to the low branching ratio of the process.
The enhancement of the statistics in the Run 2 have allowed the study of the $H \to ZZ^* \to 4l$ process in different production modes. This study has been performed developing a categorization of the selected events. It has been made classifying the events in different categories based on the production mode characteristics, and nine categories has been defined: *VH-leptonic-enriched*, *0 jet*, *1 jet* p_T^{4l}*-Low*, *1 jet* p_T^{4l}*-Med*, *1 jet* p_T^{4l}*-High*, *VBF-enriched* p_T^{j}*-Low*, *VBF-enriched* p_T^{j}*-High*, *VH-hadronic-enriched* and *ttH-enriched*. The signal composition in the first eight categories and the number of the observed and expected signal and background events are shown in Table 1. Then the *ttH-enriched* category has been studied in detail to give an estimation of the cross section in the process $pp \to ttH_{(H\to ZZ^*\to 4l)}$ using the available data.
To realize this measurement, it was important to study the contribution of the major background to the ttH production mode, the ttZ production. For this reason a Control Region with an enhanced contribution of the ttZ events has

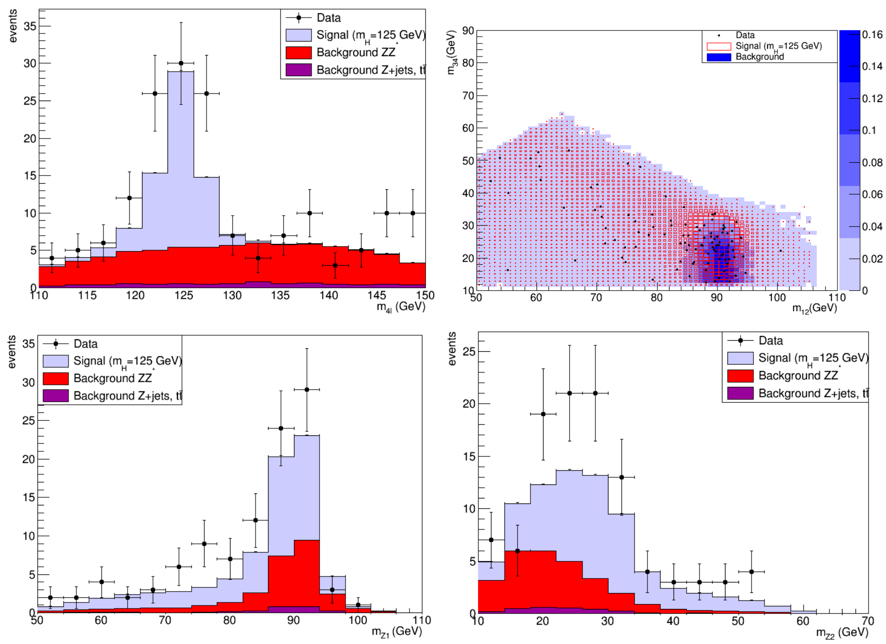

Figure 25: *On the top-left*: the distributions of the four-lepton invariant mass, m_{4l}, for the selected candidates compared to the background expectation for the $\sqrt{s} = 13$ TeV data set. The signal expectation for the m_H=125 GeV hypothesis is also shown. *On the top-right*: the distribution of the invariant mass m_{34} of the sub-leading lepton pair as a function of the invariant mass m_{12} of the leading lepton pair. The expected distribution of the SM Higgs boson with a mass of m_H=125 GeV is indicated by the size of the red boxes, while the total background is indicated by the intensity of the blues shading. *On the bottom*: the projection distribution for m_{12} (*left*) and m_{34} (*right*), labeled as m_{Z1} and m_{Z2}.

Category	**Signal Composition**	**Signal**	**Total Bkg**	**Observed**
VH-Lep	VH 83%, ttH 12%	0.318 ± 0.019	0.063 ± 0.009	0
0 jet	ggH 98%	26.8 ± 2.5	16 ± 1	49
1 jet				
Low	ggH 92%	8.8 ± 1.1	3.6 ± 0.4	12
Med	ggH 84%, VBF 12%	5.4 ± 0.7	1.26 ± 0.13	9
High	ggH 75%, VBF 18%	1.47 ± 0.24	0.184 ± 0.023	3
VH-Had	ggH 78%, VH 16%	3.54 ± 0.5	0.85 ± 0.17	3
VBF				
Low	ggH 62%, VBF 32%	6.3 ± 0.8	1.48 ± 0.33	16
High	ggH 57 %, VBF 32%	0.57 ± 0.10	0.147 ± 0.033	3

Table 1: The number of the observed and expected signal and background events in the mass range $118 < m_{4l} < 129$ GeV for an integrated luminosity of 36.1 fb^{-1} at $\sqrt{s}$=13 TeV in the other reconstructed categories.

been defined to test the agreement between data and Monte Carlo simulations. The requirements of the CR is shown in Table 2 and in Figure 26 the invariant mass distribution of the leading lepton pair, the jet multiplicity and the *missing*-E_T are presented, comparing the ttZ and the other background expectation in this CR.

Control Region	**Selection Criteria**	**Purity**
ttZ CR	At least 2 leptons that pass the nominal selection 80 GeV $< m_{l^+l^-} <$ 100 GeV and $E_T^{miss} >$ 50 GeV $N_{b-jets} \geq 1$ and $N_{jets} \geq 2$	23 %

Table 2: Selections for the ttZ Control Region.

The $t\bar{t}$ contribution in this CR has a flat distribution of the leading lepton pair, therefore it can be distinguish from the ttZ and *Z+jets*, that have a more peaked distribution around the Z boson mass of 91 GeV. The *Z+jets* presents a different distribution of the *missing*-E_T respect with the ttZ one and it allows to isolate its contribution.
The observed events are in good agreement with the expected events, as well the shape of the variable distributions, validating the Monte Carlo simulation of this process. In this way the estimation of its contribution in the ttH enriched category has been made and it results to be the larger one respect to the other background sources with 0.035 ± 0.002 events.
Finally, the expected number of signal and backgrounds events in this category had been estimated and they are shown in Table 3, together with the observed events and the signal composition of the *ttH-enriched* category.

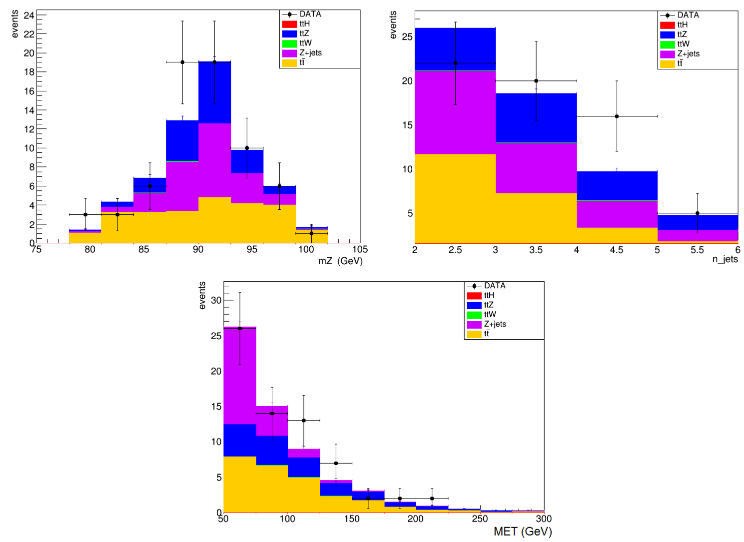

Figure 26: Invariant mass distribution of the leading lepton pair (*top-left*) and the jet multiplicity (*top-right*) and the missing-E_T (*bottom*) in the ttZ-Control Region.

Category	Signal Composition	Signal	Total Bkg	Observed
ttH	ttH 79%, ggH 13 %	0.39 ± 0.04	0.084 ± 0.04	0

Table 3: The number of the observed and expected signal and background events in the mass range $118 < m_{4l} < 129$ GeV for an integrated luminosity of 36.1 fb^{-1} at $\sqrt{s}$=13 TeV in the other reconstructed categories.

There are no observed events in the ttH enriched category. Then an upper limit on the cross section value is set. This upper limit is evaluated with a Bayesian approach and it results to be:

$$\sigma \cdot BR(H \to ZZ^*)_{obs} < 0.08 \text{ pb @ } 95\% \ C.L. \tag{6}$$

The statistical significance still limits the measurements of this process and the study of the Higgs boson coupling with the top quark to test Beyond Standard Model physics. A further enhancement of the statistics with the increasing integrated luminosity up to 100 fb^{-1} by the end of the Run 2, will allow a more accurate measurements of this coupling.

Responsabilities:

- G.Mancini Editor of the supporting documentation for the $H \to ZZ^* \to 4l$ coupling measurements

Public presentations:

- G.Mancini, "Study of the production modes of the Higgs boson and EFT interpretations in the $H \to ZZ^* \to 4l$ decay channel at 13 TeV center of mass energy with the ATLAS detector at LHC", Poster presented at IFAE 2017 (Incontri di Fisica delle Alte Energie, Trieste) (19th-21st April 2017)

- G.Mancini, "ATLAS LNF activity Status Report", Talk at the 54th Scientific Committee Meeting (13 November 2017)

- G.Mancini, "LNF Cosmic Ray Stand preliminary results with SM1 Module 0.5", Talk at the ATLAS Muon Week (NSW Performance and Testbeam) (10 November 2017)

- G.Mancini, "$H \to \gamma\gamma$ and $H \to 4l$ with 36.1 fb^{-1} at 13 TeV", Talk at the XIII ATLAS-Italy Workshop on Physics and Upgrade (25th - 27th October 2017)

- G.Mancini, "Measurement of cross sections and couplings of the Higgs Boson using the ATLAS detector", ATLAS Talk at the XXIX Recontres de Blois (28th May- 2nd June 2017)

- G.Mancini, "Study of the production modes of the Higgs boson and EFT interpretations in the $H \to ZZ^* \to 4l$ decay channel at 13 TeV center of mass energy with the ATLAS detector at LHC", Talk at the Spring Institute - Challenging the Standard Model after the Higgs discovery (12th May 2017)

Publications and internal documents:

- G.Mancini, "Measurement of cross sections and couplings of the Higgs Boson using the ATLAS detector", Proceeding of the talk at the 29th Rencontres de Blois (publishing)

- G.Mancini, "Study of the production modes of the Higgs boson and EFT interpretations in the $H \to ZZ^* \to 4l$ decay channel at 13 TeV center of mass energy with the ATLAS detector at LHC", IL NUOVO CIMENTO (publishing)

- G.Mancini, "Overview of the Higgs boson property studies at the LHC", Proceedings of Science (PP LHC 2016 012 SISSA (2016-09-21) Conference (C16-05-16.3)) (11 November 2017)

References

[1] ATLAS collaboration, New Small Wheel, Technical Design Report, CERN-LHCC-2013-006 (2013)

[2] Y. Giomataris, P. Rebourgeard, J. Robert and G. Charpak, A High granularity position sensitive gaseous detector for high particle flux environments, Nucl. Instrum. Meth. A 376 (1996) 29

[3] Measurement of the Higgs boson coupling properties in the $H \to ZZ^* \to 4l$ decay channel at $\sqrt{s} = 13$ TeV with the ATLAS detector, JHEP03 (2018) 095

[4] F. Maltoni, K. Mawatari and M. Zaro, Higgs characterisation via vector-boson fusion and associated production: NLO and parton-shower effects, Eur. Phys. J. C74 (2014) 2710, arXiv: 1311.1829 [hep-ph].

[5] Handbook of LHC Higgs Cross Sections: 4. Deciphering the Nature of the Higgs Sector (arXiv:1610.07922).